

SUPPORTING INFORMATION

Abstract: Acetato-bridged palladium-lanthanide tetranuclear heterometallic complexes of the form ($\text{Pd}_2\text{Ln}_2(\text{H}_2\text{O})_2(\text{CH}_3\text{COO})_{10}\cdot 2\text{CH}_3\text{COOH}$) ($\text{Ln}_2 = \text{Ce}_2(1)$, $\text{Pr}_2(2)$, $\text{Nd}_2(3)$, $\text{Sm}_2(4)$, $\text{Tb}_2(5)$, $\text{Dy}_2(6)$, $\text{Dy}_{0.2}\text{Y}_{1.8}(6'')$, $\text{Ho}_2(7)$, $\text{Er}_2(8)$, $\text{Er}_{0.24}\text{Y}_{1.76}(8'')$, $\text{Tm}_2(9)$, $\text{Yb}_2(10)$, $\text{Y}_2(11)$) were synthesised and characterised by experiment and theoretical techniques. All complexes containing the Kramers lanthanide ions (Ln^{3+}) ($\text{Ce}(1)$, $\text{Nd}(3)$, $\text{Sm}(4)$, $\text{Dy}(6)$, $\text{DyY}(6'')$, $\text{Er}(8)$, $\text{ErY}(8'')$, $\text{Yb}(10)$) showed field-induced slow magnetic relaxation, characteristics of single-molecule magnetic and purely of molecular origin. In contrast all synthesised non-Kramers lanthanide ions ($\text{Ln}^{3+} = \text{Pr}(2)$, $\text{Tb}(5)$, $\text{Ho}(7)$, $\text{Tm}(9)$, $\text{Y}^{3+}(11)$) is diamagnetic and non-lanthanide) did not show any slow magnetic relaxation. The variation in the electronic structure as well as accompany consequences across the complexes representing all Kramers and non-Kramers lanthanide ions were investigated. The origin of the magnetic properties and the extent to which the axial donor-acceptor interaction involving the lanthanide ions and an electron-deficient d_{z^2} of palladium affects the observed magnetic and electronic properties across the lanthanide series are presented. We report unique consistent electronic and magnetic properties of isostructural complexes spanning the lanthanide series with property variant dependent on whether the ions are Kramers or non-Kramers.

DOI: 10.1002/anie.2016XXXX

SUPPORTING INFORMATION

Table of Contents

Experimental Procedures.....	3
Characterization and Instrumental Procedures.....	3
Magnetic Measurements.....	3
Syntheses of $[(\text{PdLnAcO}_4)\text{AcO}\cdot\text{H}_2\text{O}]_2 \cdot 2\text{AcOH}$ ($\text{Ln} = \text{Ce}(1), \text{Pr}(2), \text{Nd}(3), \text{Sm}(4), \text{Tb}(5), \text{Dy}(6), \text{DyY}(6''), \text{Ho}(7), \text{Er}(8), \text{ErY}(8''), \text{Tm}(9), \text{Yb}(10), \text{Y}(11)$).....	3
General Information.....	3
Synthesis of $[(\text{PdLnAcO}_4)\text{AcO}\cdot\text{H}_2\text{O}]_2 \cdot 2\text{AcOH}$ (1-11).....	3
General equation of the reaction.....	5
Results and Discussion.....	5
Powder X-ray diffraction (PXRD) patterns.....	5
Crystal Structure.....	6
Calculation details and results.....	9
Static magnetic properties.....	11
Dynamic magnetic properties.....	12
Cole – Cole plot and relaxation time.....	16
References	18

SUPPORTING INFORMATION

Experimental Procedures

Characterization and Instrumental Procedures.

The single-crystal structure for all samples was determined using a Bruker APEX-II diffractometer with an APEX II CCD detector and graphite monochromated Mo K α radiation ($\lambda = 0.7107 \text{ \AA}$). The frames were integrated with the Bruker SAINT software package using a narrow-frame algorithm. Data were corrected for absorption effects using the multi-scan method (SADABS) while refinement and additional calculations were carried out using SHELXL-2014/7 (Sheldrick, 2014) within the APEX II interface. Intrinsic phasing was used as the refinement method. Details of each crystal are contained on each CIF file.

Using a Bruker D2 Phaser with Cu K α radiation (K α : $\lambda = 1.5402 \text{ \AA}$) radiation at room temperature powder X-ray diffraction patterns were acquired for all samples. Diffraction data were collected in the range of $5.0^\circ \leq 2\theta \leq 50.0^\circ$. Sampling and scan width was 0.02° . Raw data were stripped of K α and smoothed using EVAC SUIT software.

Elemental analyses for C and H were performed at Research and Analytical Centre for Giant Molecules, Graduate School of Science, Tohoku University, Japan on J-SCIENCE LAB CO., Ltd. JM-11 microanalyser.

FT-IR spectra of the polycrystalline samples were acquired on a JASCO FT/IR 6700 spectrometer using the ATR method using a ZnSe prism.

Inductively coupled plasma atomic emission spectrometry (ICP-AES) for yttrium diluted samples were performed to determine the stoichiometric ration of Ln-Y in diluted samples at Research and Analytical Centre for Giant Molecules, Graduate School of Science, Tohoku University, Japan on a SHIMADZU ICPE-9000 spectrometer with 5% HNO₃(aq) solution.

By using BaSO₄ as background, the UV-vis spectra were obtained on a SHIMADZU UV-3100PC UV-VIS-NIR scanning spectrophotometer in solid-state and reflectance mode. The reflectance spectra were then converted to absorbance using the Kubelka-Munk transformation.¹

Magnetic Measurements.

For each sample, the ac and dc magnetic susceptibility measurements were performed using solid polycrystalline samples on a Quantum Design MPMS-5S, MPMS controller-1822 with 5 Tesla capacity SQUID magnetometers as well as Quantum design PPMS-6000 equipped with ac-Transport controller-7100, and magnet controller-6700 with 30 Tesla capacity. The inherent diamagnetic corrections for all samples and corresponding sample holders were corrected by using Pascal's tables.² ac measurements were performed in a 3 Oe oscillating magnetic field with and without applied dc field.

Syntheses of [(PdLnAcO₄)AcO·H₂O]₂ ·2AcOH (Ln = Ce(1), Pr(2), Nd(3), Sm(4), Tb(5), Dy(6), DyY(6''), Ho(7), Er(8), ErY(8''), Tm(9), Yb(10), Y(11))

General Information.

Tripalladium(II)hexaacetate was obtained from Tokyo Chemical Industry Co. LTD while lanthanide acetate (lanthanide= Pr, Nd, Sm, Tb, Dy, Ho, Er, Tm, Yb and Y) and glacial acetic acid (99 %) were obtained from Wako Pure Chemical Industry LTD. All chemicals were used as received without further purification.

Synthesis of [(PdLnAcO₄)AcO·H₂O]₂ ·2AcOH (1-11).

Complexes 1 – 11 were synthesised according to the literature procedure.³ Pd₃(AcO)₆ (100 mg, 0.15 mmol), Ln(AcO)₃·4H₂O and glacial acetic acid (99 %, 10 mL) were refluxed in a round-bottom flask at 90 °C for 1 h. The solution obtained was

SUPPORTING INFORMATION

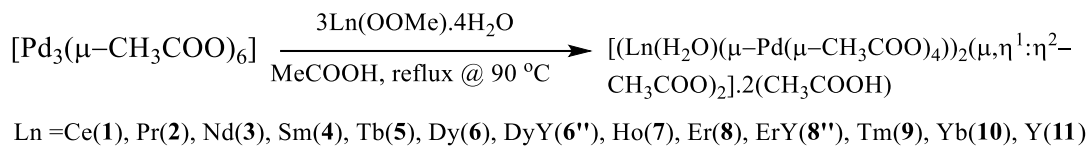
concentrated to 5 mL and slowly cooled in the bath to room temperature. The solution was then filtered and layered with diethyl ether. The crystal obtained was used for all other characterisations. Table S1 contain a summary of the mass of $\text{Ln}(\text{AcO})_3 \cdot 4\text{H}_2\text{O}$ used for the synthesis, yield, elemental analysis and IR spectrum for each complex.

Table S1: Summary of the mass of $\text{Ln}(\text{AcO})_3 \cdot 4\text{H}_2\text{O}$ used for the synthesis, yield, elemental analysis and IR spectrum for each complex.

Complex	Mass of $\text{Ln}(\text{AcO})_3 \cdot 4\text{H}_2\text{O}$	Yield based on Ln	Anal. for $\text{Pd}_2\text{Ln}_2\text{C}_{24}\text{O}_{26}\text{H}_{42}$		IR spectrum (ATR, ν/cm^{-1})
			Calc. (%):	Found (%)	
1 (Ce)	175 mg 0.45 mmol	248 mg 89 %	C, 23.25 H, 3.42	C, 23.66 H, 3.82	3397br, 3266w, 2937w, 2632w, 1684m, 1619vs, 1539s, 1406vs, 1344m, 1283m, 1050m, 1020m, 952w, 692vs, 622s
2 (Pr)	175.55 mg 0.45 mmol	243 mg 87 %	C, 23.22 H, 3.41	C, 23.66 H, 3.86	3285br, 3166w, 1695m, 1654m, 1539vss, 1454vs, 1414s, 1051m, 1017m, 968m, 945w, 681vs, 604m
3 (Nd)	177.04 mg 0.45 mmol	258 mg 92 %	C, 23.10 H, 3.39	C, 22.88 H, 3.88	3683w, 3390br, 2969w, 2865w, 2356w, 1616s, 1558s, 1543s, 1384vs, 1334m, 1052s, 1022s, 844w, 775w, 686vs, 617s
4 (Sm)	179.80 mg 0.45 mmol	255 mg 90 %	C, 22.88 H, 3.36	C, 22.60 H, 3.42	3394br, 3262w, 3008w, 2931w, 2634w, 2553w, 1685m, 1619vs, 1535s, 1400vs, 1346m, 1280m, 1018m, 944w, 867w, 682vs, 620s
5 (Tb)	183.65 mg 0.45 mmol	255 mg 90 %	C, 22.57 H, 3.31	C, 22.42 H, 3.38	3397br, 3268w, 3019w, 2630w, 1683m, 1620vs, 1539s, 1405vs, 1345m, 1279m, 1050m, 1020m, 952w, 885w, 691vs, 622s
6 (Dy)	185.26 mg 0.45 mmol	236 mg 92%	C, 22.44 H, 3.30	C, 22.44 H, 3.28	3392br, 3266w, 3005w, 2938w, 2633w, 2555w, 1683m, 1619vs, 1538s, 1407vs, 1346m, 1282m, 1049m, 1019m, 953w, 871w, 689vs, 622s
7 (Ho)	186.35 mg 0.45 mmol	264 mg 91 %	C, 22.36 H, 3.28	C, 22.38 H, 3.40	3375br, 3289w, 3017w, 2934w, 1687m, 1610w, 1538vs, 1418vs, 1341m, 1247m, 1051m, 1020m, 946w, 673vs, 645s, 608s
8 (Er)	187.40 mg 0.45 mmol	262 mg 90 %	C, 22.28 H, 3.27	C, 22.34 H, 3.28	3397br, 3262w, 2989w, 2930w, 2553w, 1685m, 1623vs, 1538s, 1403vs, 1346w, 1276m, 1014m, 952w, 871w, 825w, 682vs, 620s
9 (Tm)	188.16 mg 0.45 mmol	263 mg 90 %	C, 22.22 H, 3.26	C, 22.28 H, 3.28	3406br, 3266w, 3018w, 2943w, 2578w, 1698s, 1594vs, 1540s, 1466vs, 1348m, 1280m, 1042m, 1018m, 958w, 875w, 681vs, 619s
10 (Yb)	190.46 mg 0.45 mmol	273 mg 93 %	C, 22.08 H, 3.24	C, 22.12 H, 3.28	3417 br, 3016w, 2935w, 1687m, 1627vs, 1573s, 1396vs, 1342m, 1280m, 1114m, 1022m, 952w, 883w, 682vs, 613s
11 (Y)	152.15 mg 0.45 mmol	228 mg 89 %	C, 25.35 H, 3.72	C, 25.46 H, 3.86	3404br, 3265w, 3006w, 2939w, 2623w, 2542w, 1685m, 1622vs, 1540s, 1407vs, 1346m, 1282m, 1047m, 1020m, 955w, 881w, 690vs, 622s
6'' ($\text{Dy}_{0.1}\text{Y}_{0.9}$)	Dy 16.47 mg 0.04 mmol Y 138.3 mg 0.41 mmol	231 mg 88 %	C, 24.71 H, 3.63	C, 25.02 H, 3.72	3397br, 3273w, 3018w, 2946w, 2638w, 2547w, 1648m, 1621vs, 1539s, 1407vs, 1345m, 1282m, 1050m, 1019m, 954w, 691vs, 617s
8'' ($\text{Er}_{0.12}\text{Y}_{0.88}$)	Er 16.66 mg 0.04 mmol Y 138.3 mg 0.41 mmol	231 mg 88 %	C, 24.67 H, 3.62	C, 254.82 H, 3.72	3393w, 3296br, 3018w, 2940w, 2633w, 1687m, 1623vs, 1540s, 1407vs, 1345m, 1283m, 1049m, 1021m, 955w, 882w, 691vs, 622s

SUPPORTING INFORMATION

General equation of the reaction.



Results and Discussion

Powder X-ray diffraction (PXRD) patterns.

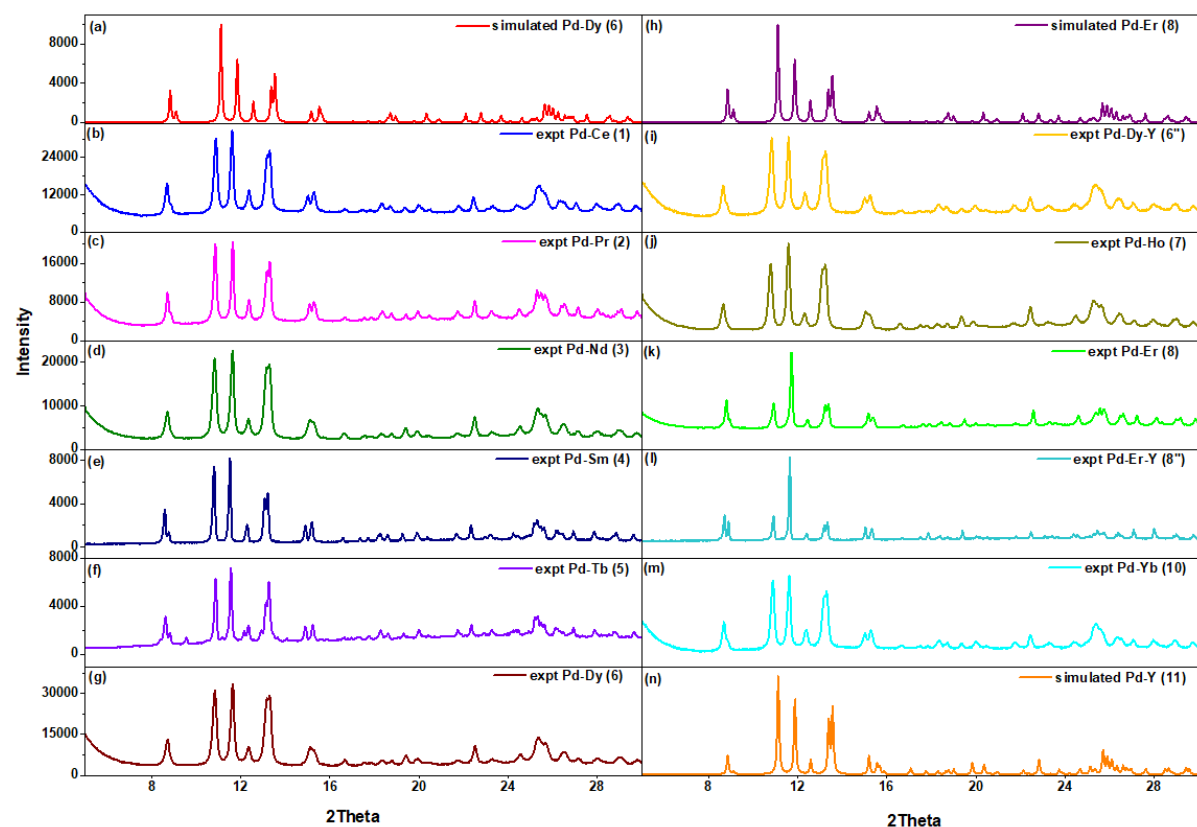


Figure S1. The powder X-ray diffraction pattern of (a) **6** simulated from single crystal X-ray diffraction (b) **1** from experiment (c) **2** from experiment (d) **3** from experiment (e) **4** from experiment (f) **5** from experiment (g) **6** from experiment (h) **8** simulated from single crystal structure of **8** (i) **6''** from experiment (j) **7** from experiment (k) **8** from experiment (l) **8''** from experiment (m) **10** from experiment (n) **11** simulated from single crystal X-ray diffraction Cu K α : $\lambda = 1.5402 \text{ \AA}$

The powder patterns show the absence of polymorphs and no phase transition between the single crystal and the polycrystalline samples. Peak indexing was not carried out on the experimental pattern since the powder patterns from the experiment (Figure S1b-g, S1i-m) perfectly matched the simulated (Figure S1a, S1h, and S1n). The samples are highly crystalline which is evident from the sharp peak at lower 2theta angles.

SUPPORTING INFORMATION

Crystal Structure

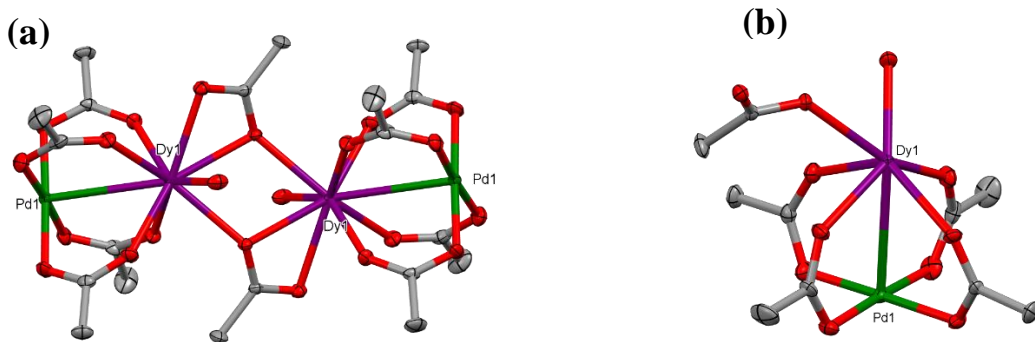


Figure S2. (a) Crystal structure of **6** (b) the asymmetric unit for **6** (50 % probability) (Grey = C, green = Pd, purple = Dy, red = O. Hydrogen atoms were omitted for clarity)

Table S2. Selected crystal data for **5**, **6**, **7** and **8**

Parameter	5	6	7	8
Radiation type, wavelength/Å	Mo K α , 0.71073			
Molecular formula	C ₂₄ H ₄₂ Tb ₂ O ₂₆ Pd ₂	C ₂₄ H ₄₂ O ₂₆ Pd ₂ Dy ₂	C ₂₄ H ₄₂ Ho ₂ O ₂₆ Pd ₂	C ₂₄ H ₄₂ O ₂₆ Pd ₂ Er ₂
Formula mass / gmol ⁻¹	1277.24	1284.37	1289.23	1293.89
Space group	<i>P</i> 2 ₁ / <i>n</i>			
Crystal system	Monoclinic			
<i>a</i> / Å	8.7229(4)	8.7311(7)	8.7236(4)	8.7293(9)
<i>b</i> / Å	19.4527(8)	19.4472(15)	19.4115(10)	19.390(2)
<i>c</i> / Å	11.7072(5)	11.6834(9)	11.6820(6)	11.6462(12)
$\alpha = \gamma / {}^\circ$	90			
$\beta / {}^\circ$	90.860(1)	90.819(2)	90.862(1)	90.905(2)
$V / \text{\AA}^3$	1986.30(15)	1983.6(3)	1977.99(17)	1971.0(4)
<i>T</i> / K	296			
<i>Z</i>	2			
GOF on F ²	1.070	0.918	1.074	0.785
<i>R</i> ₁ , <i>wR</i> ₂ [<i>I</i> > 2σ(<i>I</i>)]	0.0237, 0.0420	0.0457, 0.1307	0.0228, 0.0432	0.0276, 0.0924
<i>R</i> ₁ , <i>wR</i> ₂ [all data]	0.0326, 0.0439	0.0520, 0.1381	0.0289, 0.0446	0.0349, 0.1010
θ range for data collection / °	2.02 to 34.97	2.02 to 34.74	2.04 to 34.87	2.01 to 26.09
<i>R</i> int / %	2.37	4.57	2.28	2.76

SUPPORTING INFORMATION

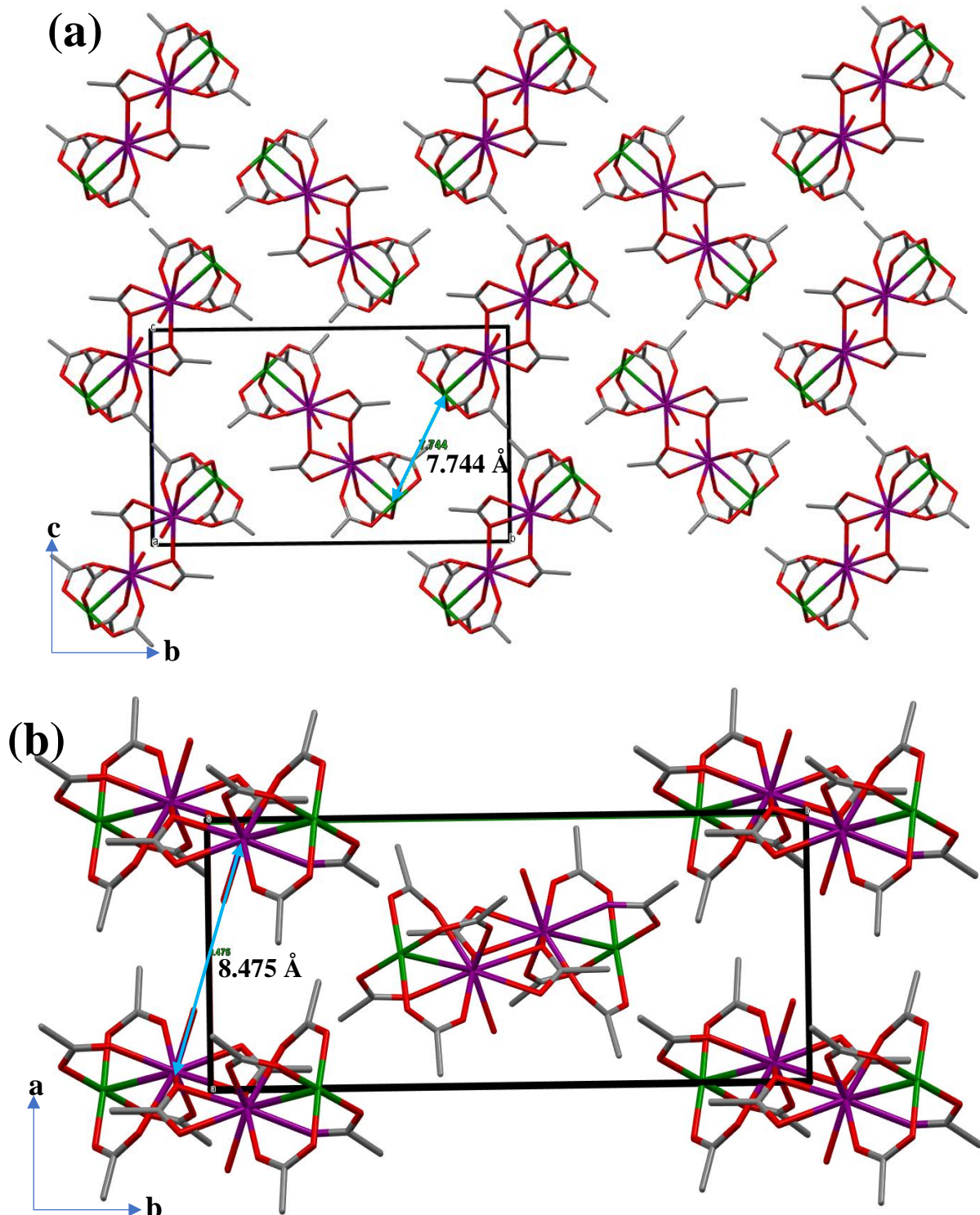


Figure S3. Crystal packing of compound **6** (a) showing the shortest intermolecular Pd-Dy distance in *cb*-plane (b) showing the shortest intermolecular Dy-Dy distance on the *ab*-plane (Dark blue double-headed arrows)

SUPPORTING INFORMATION

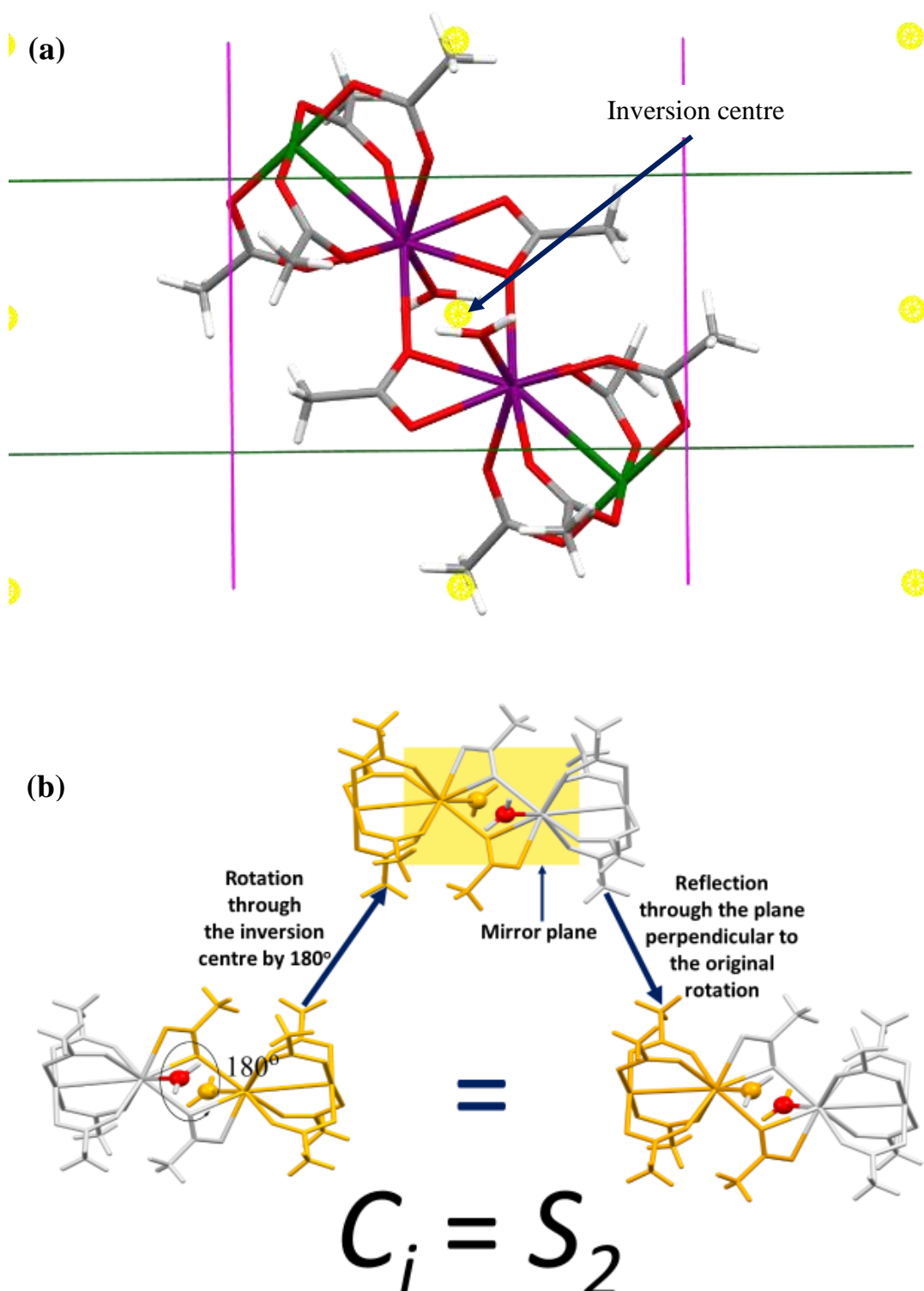


Figure S4. Crystal structure of **6** showing (a) centre of inversion (yellow spots) and (b) 2-fold improper rotation scheme of **6** (The oxygen is coloured for clarity)

SUPPORTING INFORMATION

Calculation details and results

The time-dependent density functional theory (TDDFT) as implemented in Orca software package⁴ was employed at the ωB97X-D3 level⁵ which utilises the atom-pairwise dispersion correction with the zero-damping scheme (D30)⁵ and automatic generation of auxiliary basis sets⁶ for all atoms. The density fitting was performed by employing the resolution of identity (RI) approximation for the coulombic integral (J), and numerical integration for the Hartree-Fock exchange (COSX) put as RIJCOSX.⁷ DEF2-TZVP basis (C, O, H, Pd, Dy) and effective core potential (ECP) (28 core electrons for Pd and Dy) were obtained from the Basis set Exchange library.⁸ Visualisation of the molecular orbitals was achieved by using both Gabedit 2.5.0 and Chimera 1.14rc software package.^{9,10}

Table S3. selected orbital occupation in the alpha and beta space involved transitions

MO	α – space		α + β	MO	β – space	
	Occupation (electron)	Orbital Energy (eV)			Occupation (electron)	Orbital Energy (eV)
αHOMO-20	1	-10.7638	2	βHOMO-10	1	-10.143
αHOMO-19	1	-10.6727	2	βHOMO-9	1	-10.1373
αHOMO-18	1	-10.6447	2	βHOMO-8	1	-10.0919
αHOMO-17	1	-10.5626	2	βHOMO-7	1	-9.8094
αHOMO-16	1	-10.5204	2	βHOMO-6	1	-9.8053
αHOMO-15	1	-10.4332	2	βHOMO-5	1	-9.7208
αHOMO-14	1	-10.3915	2	βHOMO-4	1	-9.717
αHOMO-13	1	-10.3465	2	βHOMO-3	1	-9.594
αHOMO-12	1	-10.297	2	βHOMO-2	1	-9.5863
αHOMO-11	1	-10.2063	2	βHOMO-1	1	-9.0923
αHOMO-10	1	-10.1404	2	βHOMO	1	-9.0844
αHOMO-9	1	-10.1265	1	βLUMO	0	0.6625
αHOMO-8	1	-10.0834	1	βLUMO+1	0	0.666
αHOMO-7	1	-9.8092	1	βLUMO+2	0	1.5127
αHOMO-6	1	-9.8038	1	βLUMO+3	0	1.565
αHOMO-5	1	-9.7199	1	βLUMO+4	0	1.6368
αHOMO-4	1	-9.717	1	βLUMO+5	0	1.683
αHOMO-3	1	-9.5905	1	βLUMO+6	0	1.7104
αHOMO-2	1	-9.5764	1	βLUMO+7	0	1.8327
αHOMO-1	1	-9.0964	1	βLUMO+8	0	2.0798
αHOMO	1	-9.089	1	βLUMO+9	0	2.1304
αLUMO	0	-0.4351	0	βLUMO+10	0	2.1637
αLUMO+1	0	-0.2323	0	βLUMO+11	0	2.2769
αLUMO+2	0	0.6601	0	βLUMO+12	0	2.3536
αLUMO+3	0	0.6642	0	βLUMO+13	0	2.4758
αLUMO+4	0	1.5556	0	βLUMO+14	0	2.569

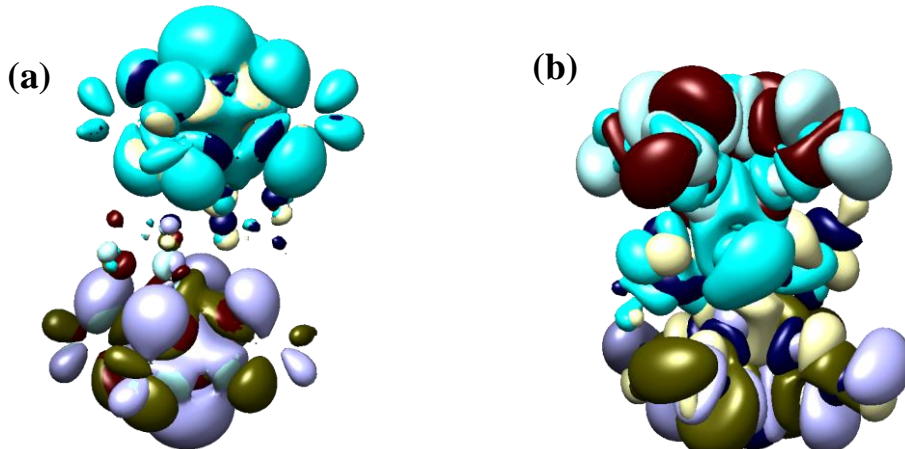


Figure S5. Molecular orbital of **6** showing (a) Highest occupied molecular orbital involving the full molecular unit with Pd-Dy bonding interaction (b) lowest unoccupied molecular orbital involving the full molecular unit with Dy hybrid s and f-orbitals interactions with oxygen

SUPPORTING INFORMATION

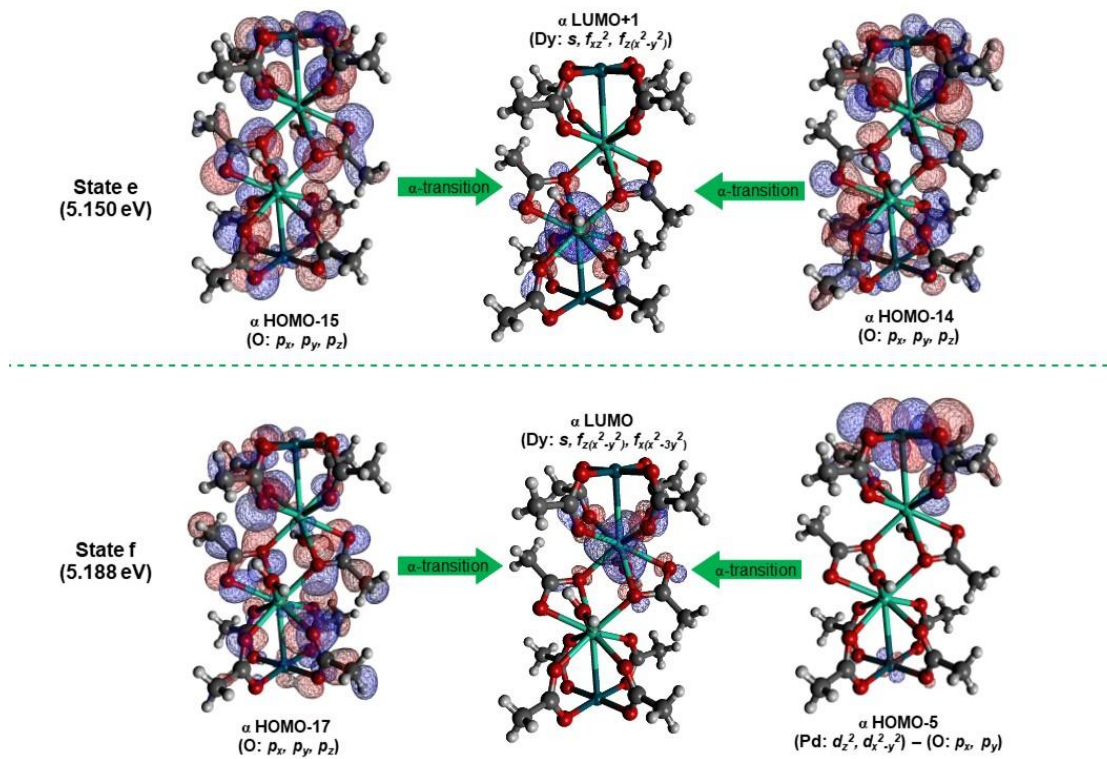


Figure S6. Molecular orbital mapping of **6** showing orbital contributions to the transitions at 5.150 and 5.188 eV at states e and state f from TDDFT (green arrow: α -transitions)

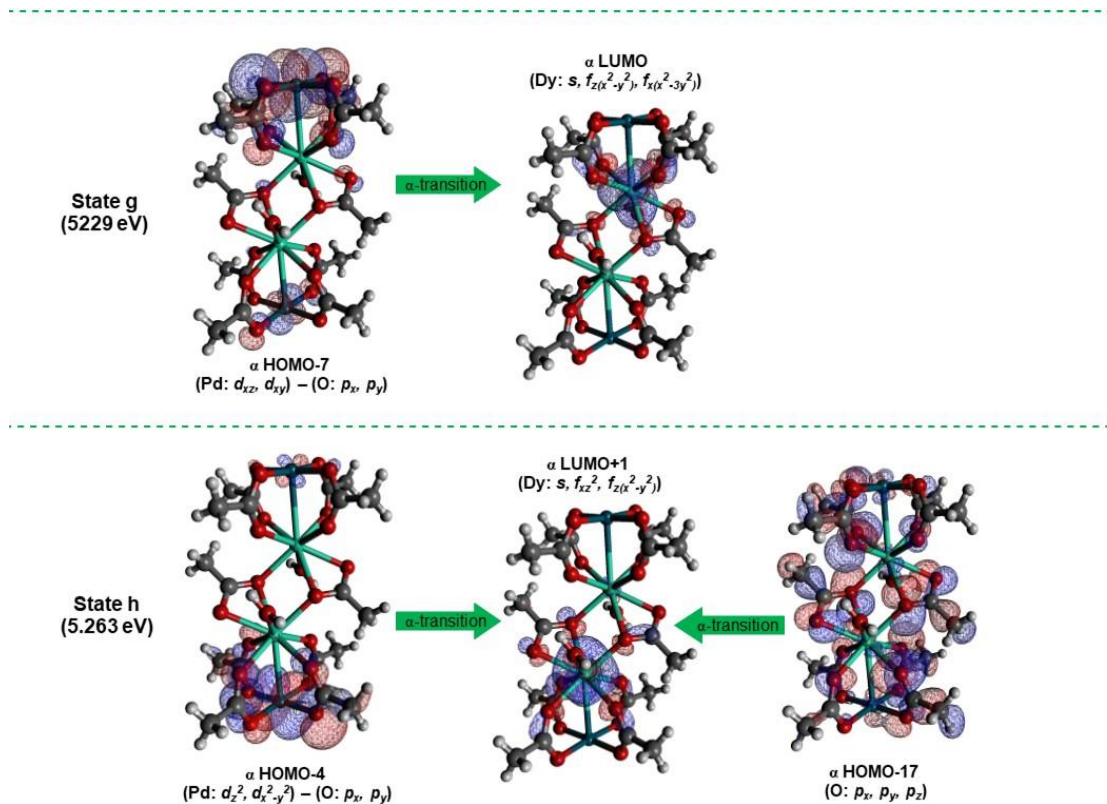


Figure S7. Molecular orbital mapping of **6** showing orbital contributions to the transitions at 5.229 and 5.263 eV at states g and h from TDDFT (green arrow: α -transitions)

SUPPORTING INFORMATION

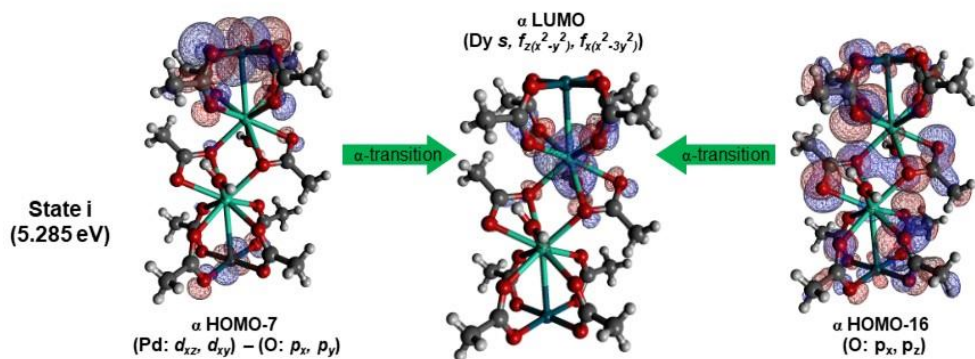


Figure S8. Molecular orbital mapping of **6** showing orbital contributions to the transitions at 5.285 eV at state i from TDDFT (green arrow: α -transitions)

Static magnetic properties

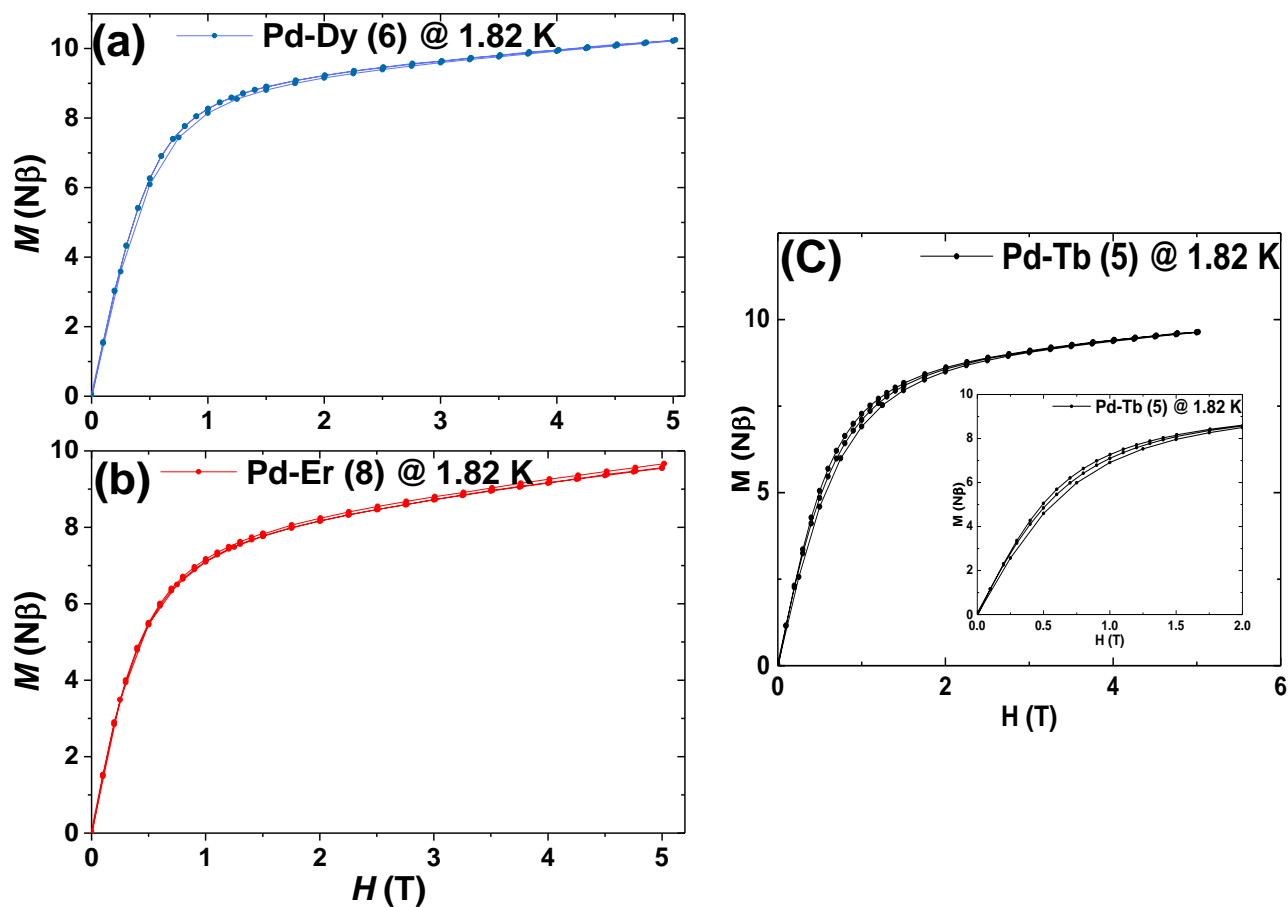


Figure S9. M vs H plots for (a) complex **6** at 1.82 K (b) complex **8** at 1.82 K

SUPPORTING INFORMATION

Dynamic magnetic properties

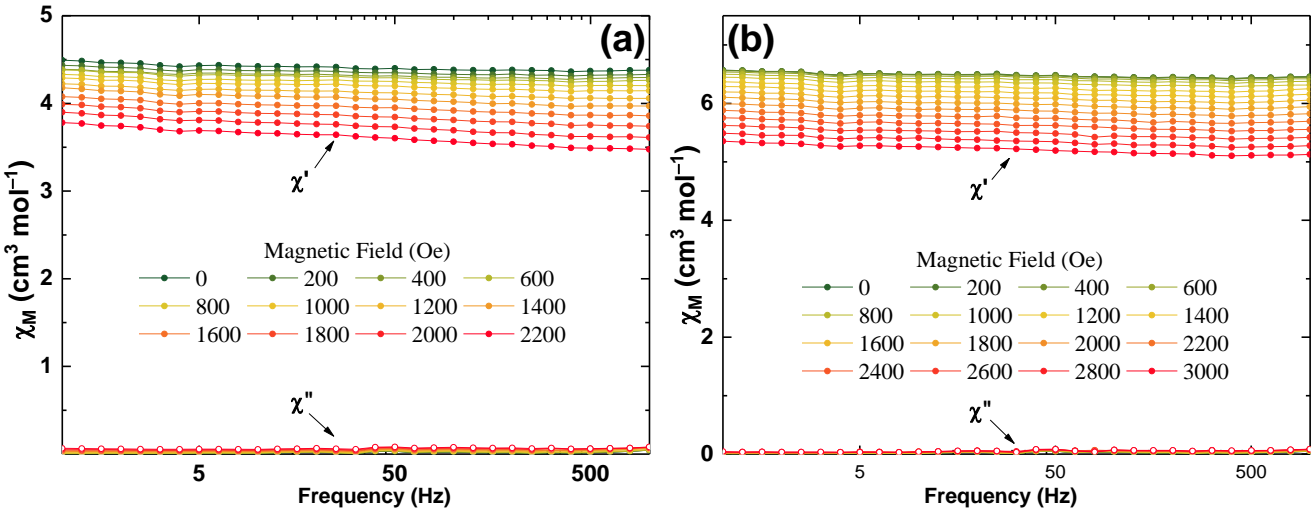


Figure S10. Field scan of the magnetic susceptibility showing no frequency dependency for (a) complex Pd-Ho (7), in-phase and out-of-phase at 1.85 K (b) complex Pd-Tb (5), in-phase and out-of-phase at 2 K

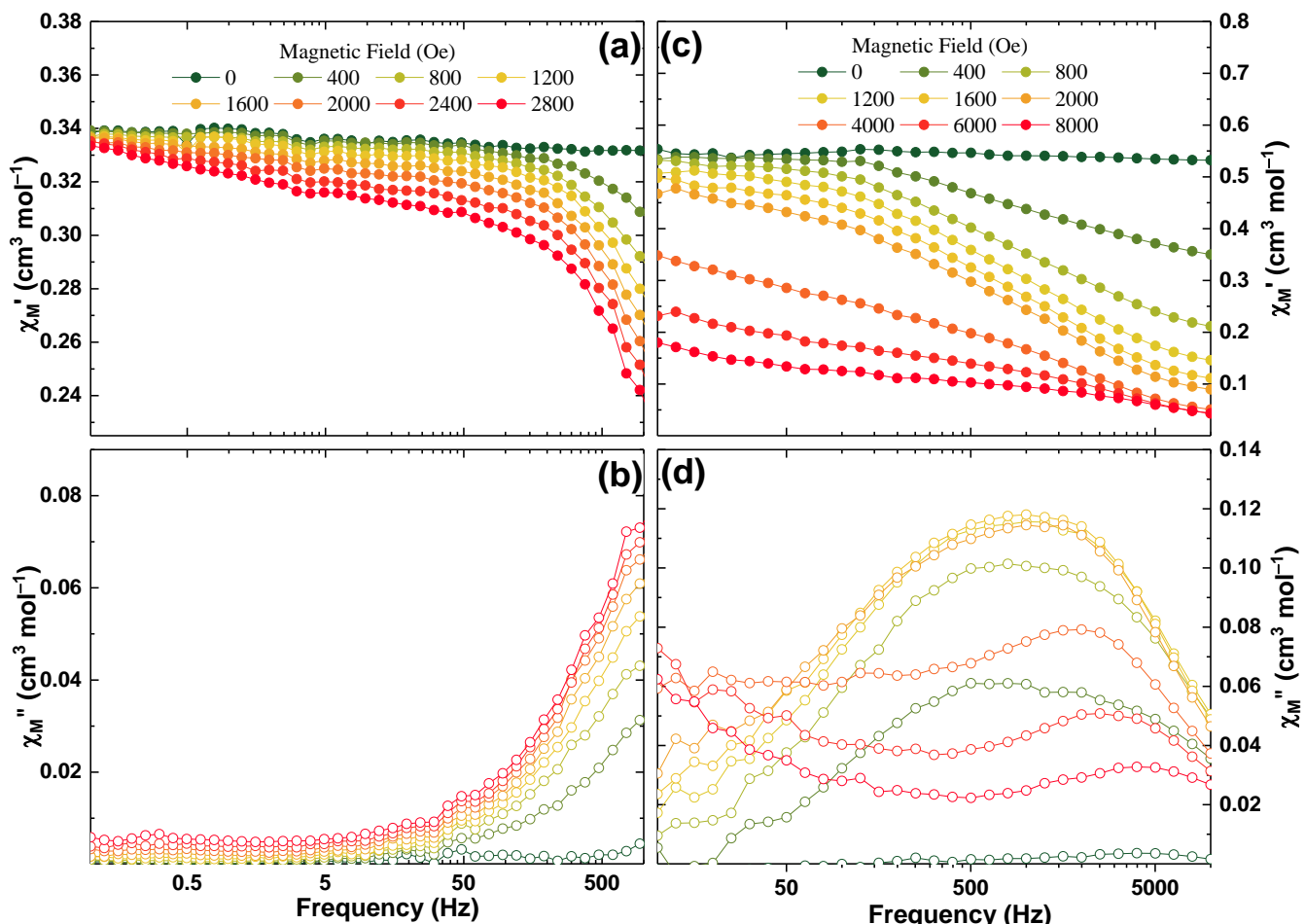


Figure S11. Field scan of the magnetic susceptibility for (a) Complex Pd-Ce (1), in-phase at 2 K and 0 – 2800 Oe (b) Complex Pd-Ce (1), out-of-phase at 2 K and 0 – 2800 Oe (c) Complex Pd-Nd (3), in-phase at 2 K and 0 – 4800 Oe (d) Complex Pd-Nd (3), out-of-phase at 2K and 0 – 4800 Oe

SUPPORTING INFORMATION

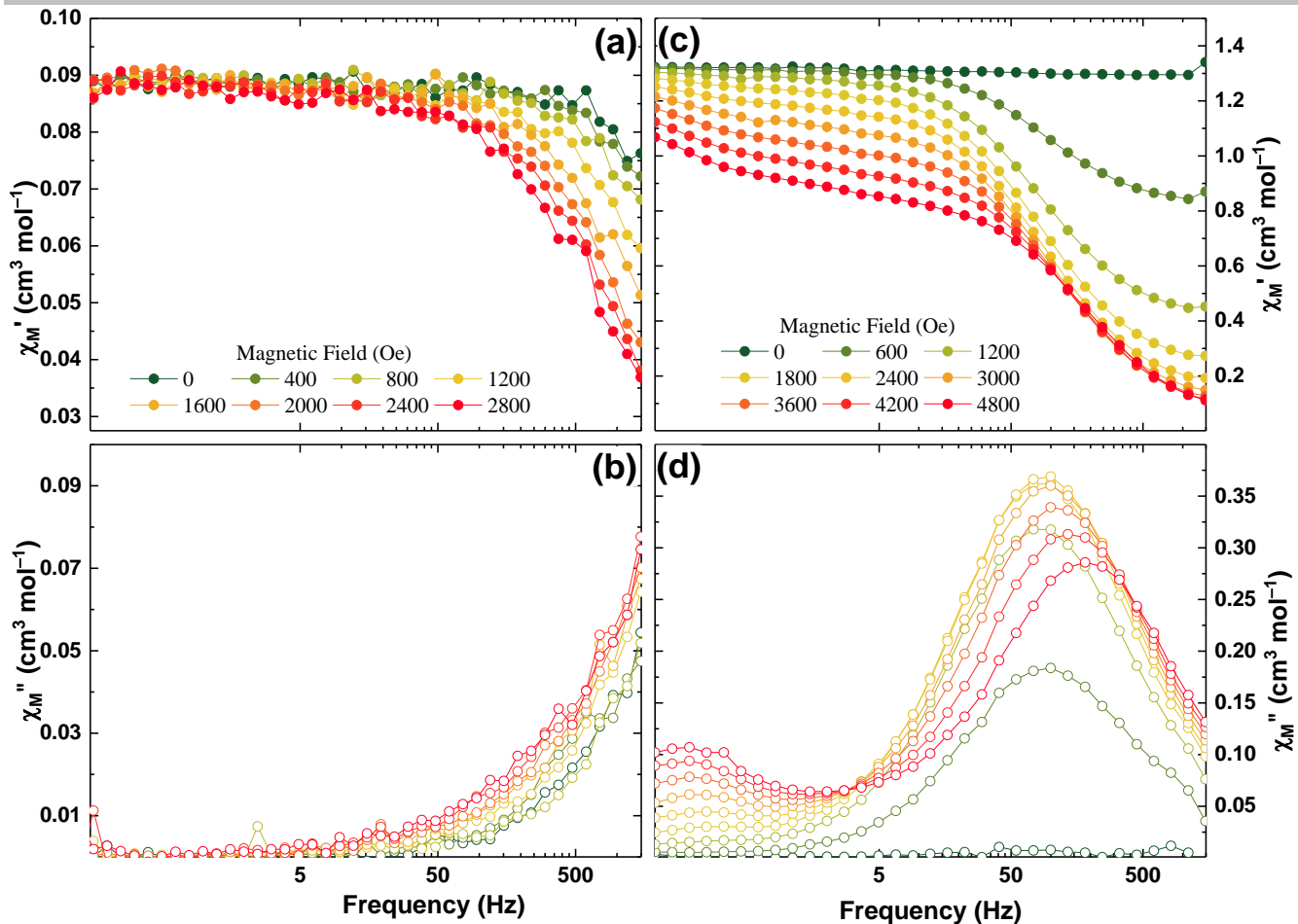


Figure S12. Field scan of the magnetic susceptibility for (a) Complex Pd-Sm (4), in-phase at 1.85 K and 0 – 2800 Oe (b) Complex Pd-Sm (4), out-of-phase at 1.85 K and 0 – 2800 Oe (c) Complex Pd-Yb (10), in-phase at 2 K and 0 – 4800 Oe (d) Complex Pd-Yb (10), out-of-phase at 2 K and 0 – 4800 Oe

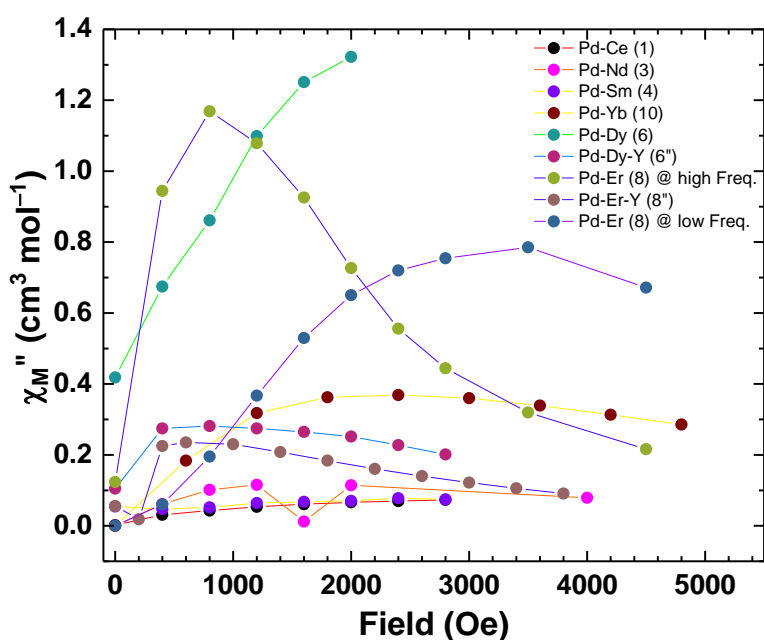


Figure S13. Optimum field vs out-of-phase susceptibility plot for 1, 3, 4, 6, 6'', 8, 8'' and 10. (Each line represents a trace of maximum intensity of out-of-phase magnetic susceptibility measured for each field for the corresponding complex. The optimum field is, therefore, the point on each line with the highest susceptibility value).

SUPPORTING INFORMATION

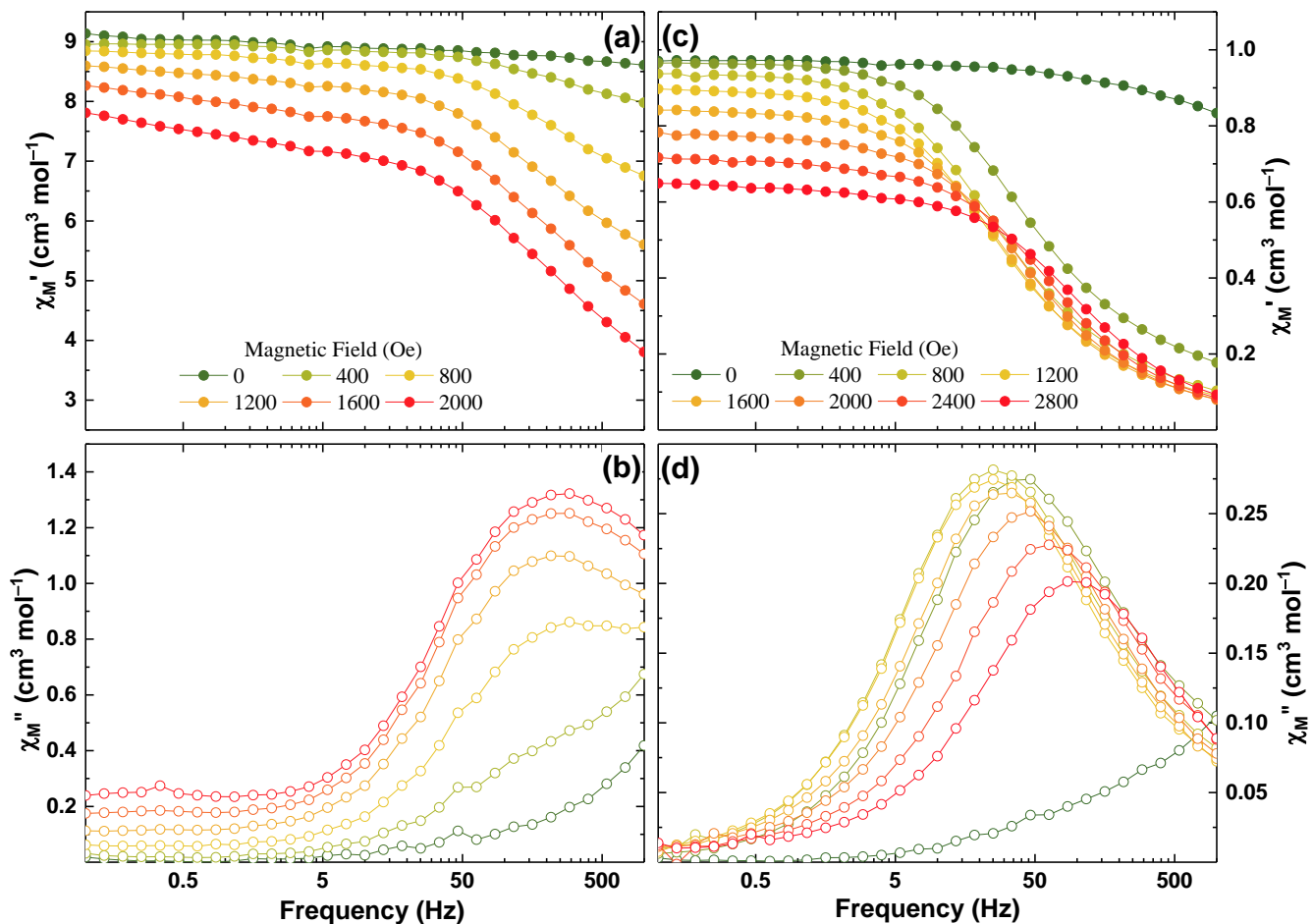


Figure S14. Field scan of the magnetic susceptibility for (a) Complex Pd-Dy (**6**), in-phase at 1.85 K and 0 – 2000 Oe (b) Complex Pd-Dy (**6**), out-of-phase at 1.85 K and 0 – 2000 Oe (c) Complex Pd-Dy-Y (**6''**), in-phase at 1.85 K and 0 – 2800 Oe (d) Complex Pd-Dy-Y (**6''**), out-of-phase at 1.85 K and 0 – 2800 Oe

SUPPORTING INFORMATION

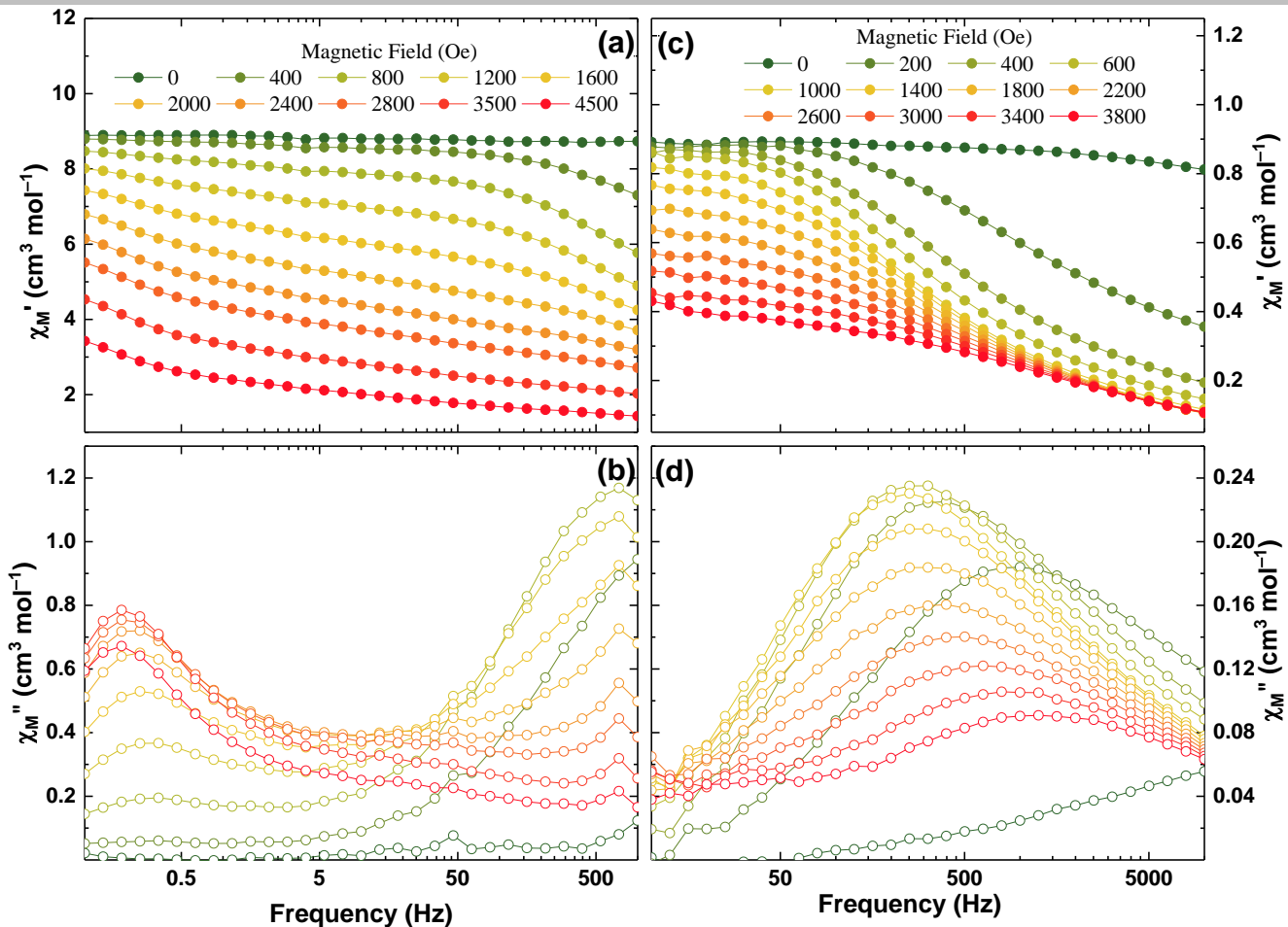


Figure S15. Field scan of the magnetic susceptibility for (a) Complex Pd-Er (8), in-phase at 1.85 K and 0 – 4500 Oe (b) Complex Pd-Er (8), out-of-phase at 1.85 K and 0 – 4500 Oe (c) Complex Pd-Er-Y (8''), in-phase at 2 K and 0 – 3800 Oe (d) Complex Pd-Er-Y (8''), out-of-phase at 2 K and 0 – 3800 Oe

SUPPORTING INFORMATION

Cole – Cole plot and relaxation time

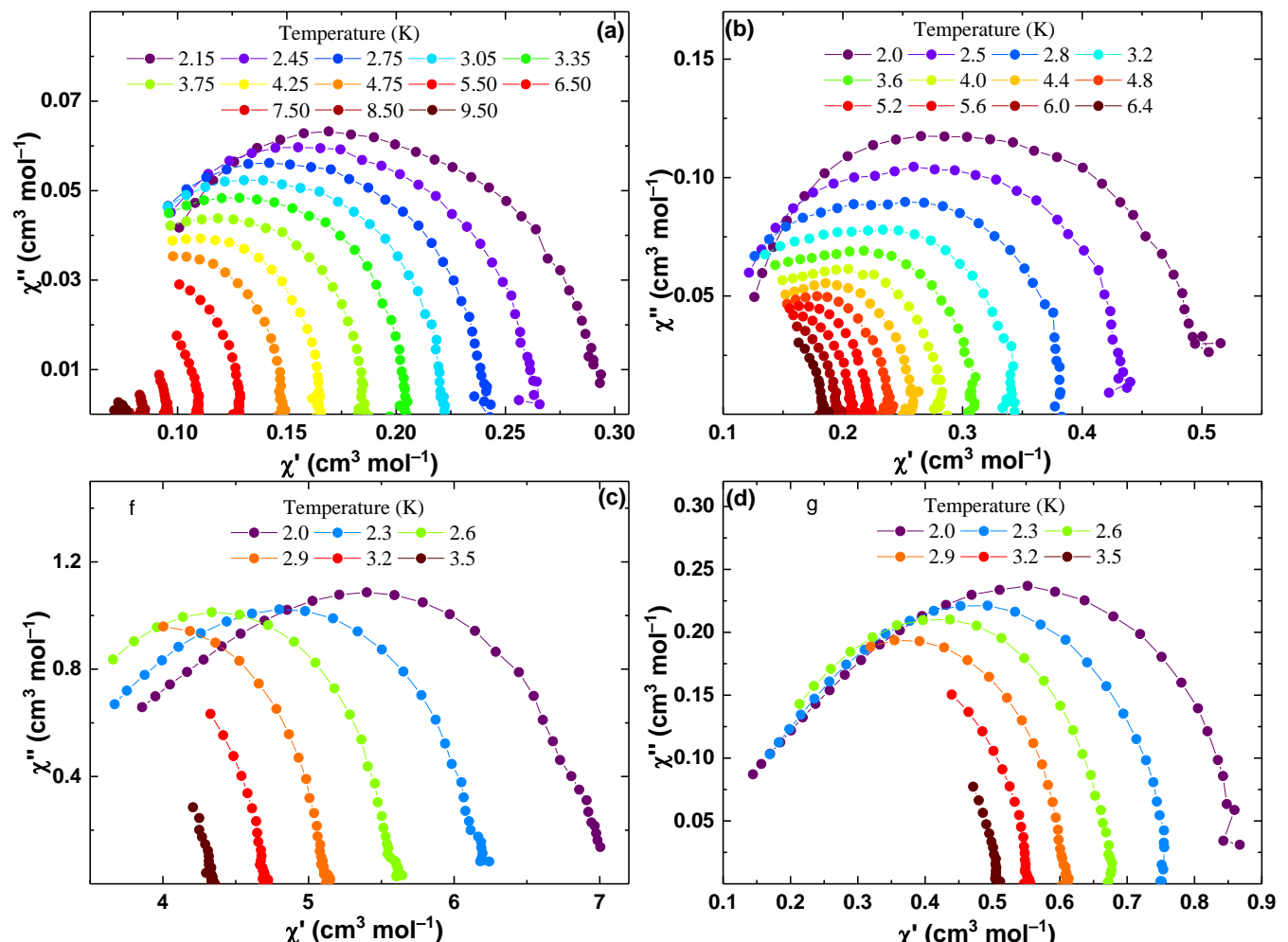


Figure S16. Cole-Cole plot for (a) compound Pd-Ce (**1**) at 2600 Oe (b) compound Pd-Nd (**3**) at 1400 Oe (c) compound Pd-Er (**8**) at 800 Oe (d) compound Pd-Er-Y (**8''**) at 600 Oe

SUPPORTING INFORMATION

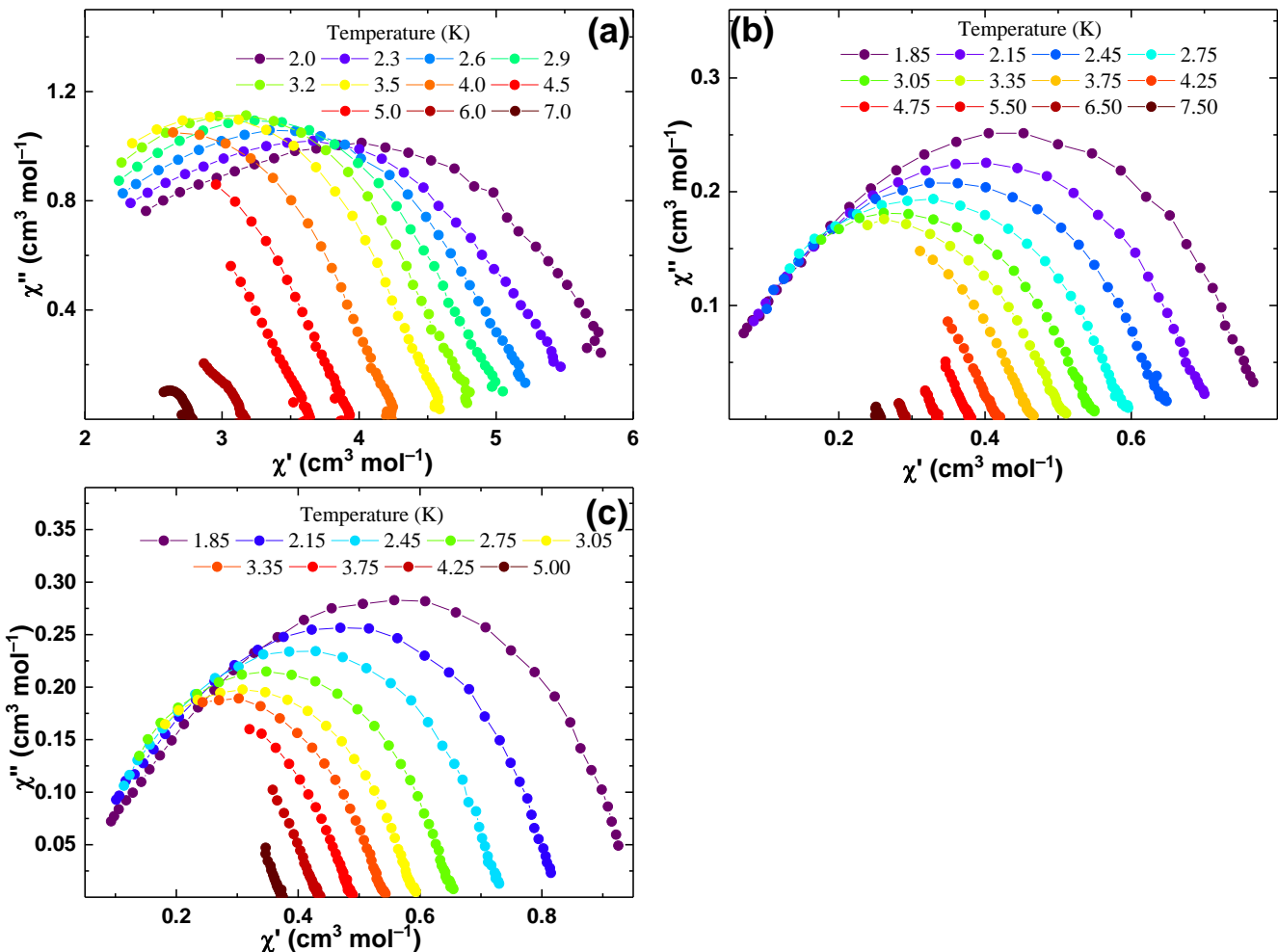


Figure S17. Cole-Cole plot for (a) compound Pd-Dy (**6**) at 2000 Oe (b) compound Pd-Dy-Y (**6''**) at 2000 Oe (c) compound Pd-Dy-Y (**6''**) at 800 Oe

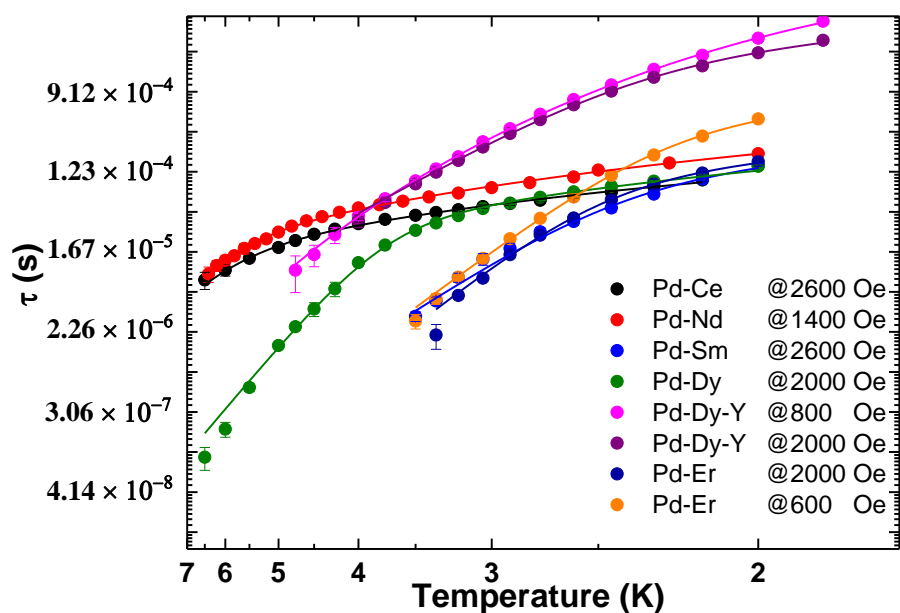


Figure S18. Relaxation time vs Temperature plot for compound Pd-Ce (**1**) at 2600 Oe, Pd-Nd (**3**) at 1400 Oe, Pd-Sm (**4**) at 2600 Oe, Pd-Dy (**6**) at 2000 Oe, Pd-Dy-Y (**6''**) at 2000 Oe, Pd-Dy-Y (**6''**) at 800 Oe, Pd-Er (**8**) at 800 Oe and Pd-Er-Y (**8''**) at 600 (The lines are fits for the respective sample plots)

SUPPORTING INFORMATION

References

- (1) Kubelka, P.; Munk, F. Ein Beitrag Zur Optik Der Farbanstriche. *Zeitschrift für Tech. Phys.* **1931**, *12*, 593–601. <https://doi.org/10.4236/msce.2014.28004>.
- (2) Bain, G. A.; Berry, J. F. Diamagnetic Corrections and Pascal's Constants. *J. Chem. Educ.* **2008**, *85* (4), 532–536. <https://doi.org/10.1021/ed085p532>.
- (3) Nefedov, S. E.; Kozitsyna, N. Y.; Vargaftik, M. N.; Moiseev, I. I. Palladium(II)-Rare-Earth Metal(III) Paddlewheel Carboxylate Complexes: Easy Total Acetate to Pivalate Metathesis. *Polyhedron* **2009**, *28* (1), 172–180. <https://doi.org/10.1016/j.poly.2008.10.006>.
- (4) Neese, F. The ORCA Program System. *Wiley Interdiscip. Rev. Comput. Mol. Sci.* **2012**, *2* (1), 73–78. <https://doi.org/10.1002/wcms.81>.
- (5) Grimme, S.; Antony, J.; Ehrlich, S.; Krieg, H. A Consistent and Accurate Ab Initio Parametrization of Density Functional Dispersion Correction (DFT-D) for the 94 Elements H-Pu. *J. Chem. Phys.* **2010**, *132* (15), 154104. <https://doi.org/10.1063/1.3382344>.
- (6) Stoychev, G. L.; Auer, A. A.; Neese, F. Automatic Generation of Auxiliary Basis Sets. <https://doi.org/10.1021/acs.jctc.6b01041>.
- (7) Neese, F.; Wennmohs, F.; Hansen, A.; Becker, U. Efficient, Approximate and Parallel Hartree–Fock and Hybrid DFT Calculations. A 'Chain-of-Spheres' Algorithm for the Hartree–Fock Exchange. *Chem. Phys.* **2009**, *356* (1–3), 98–109. <https://doi.org/10.1016/j.chemphys.2008.10.036>.
- (8) Pritchard, B. P.; Altarawy, D.; Didier, B.; Gibson, T. D.; Windus, T. L. New Basis Set Exchange: An Open, Up-to-Date Resource for the Molecular Sciences Community. *J. Chem. Inf. Model.* **2019**, *59* (11), 4814–4820. <https://doi.org/10.1021/acs.jcim.9b00725>.
- (9) Allouche, A.-R. Gabedit-A Graphical User Interface for Computational Chemistry Softwares. *J. Comput. Chem.* **2011**, *32* (1), 174–182. <https://doi.org/10.1002/jcc.21600>.
- (10) Pettersen, E. F.; Goddard, T. D.; Huang, C. C.; Couch, G. S.; Greenblatt, D. M.; Meng, E. C.; Ferrin, T. E. UCSF Chimera?A Visualization System for Exploratory Research and Analysis. *J. Comput. Chem.* **2004**, *25* (13), 1605–1612. <https://doi.org/10.1002/jcc.20084>.